Rost, S., Weber, M. (2001): A reflector at 200 km depth beneath the northwest Pacific. - Geophysical Journal International, 147, 1, pp. 12—28.

DOI: http://doi.org/10.1046/j.1365-246X.2001.00497.x

Geophys. J. Int. (2001) **147,** 12–28

A reflector at 200 km depth beneath the northwest Pacific

S. Rost[1,*] and M. Weber[2,†]

[1] *Universität Göttingen, Institut für Geophysik, Herzberger Landstr.* 180, D–37075 *Göttingen, Germany. E-mail: srost@uni-geophys.gwdg.de*
[2] *GeoForschungsZentrum Potsdam, Telegrafenberg,* D–14473 *Potsdam, Germany. E-mail: mhw@gfz-potsdam.de*

Accepted 2001 April 24. Received 2001 April 23; in original form 2000 July 19

SUMMARY

We present an analysis of precursors to *PP* produced by underside reflections from discontinuities in the upper mantle beneath the NW Pacific. The events used for this study occur in the western Pacific Rim (New Zealand, Fiji, Tonga, Solomon, New Guinea, Philippine Islands) and are recorded at the short-period Yellowknife Array (YKA) in northern Canada. The source–receiver combination results in *PP* reflection points which allow us to study the upper mantle structure in a corridor from the Hawaiian Islands to the Kuril subduction zone. To detect the weak precursors in the time window between the *P* arrival and the *PP* onset and to identify them as *PP* underside reflections, special array techniques are used. Our analysis indicates a reflector at a depth of ~200 km beneath the northwestern Pacific. This reflector shows strong topography of some tens of kilometres on length scales of several hundred kilometres, complicating the detection of this reflector in global or regional stacks of seismograms. Different models for the impedance jump across the reflector, the thickness and the possible fine structure of the reflector are modelled using synthetic seismograms and are compared with the data. The thickness of the reflector has to be less than 7 km and the *P* wave impedance contrast has to be larger than 5.0–6.5 per cent to be detected by this study. This corresponds to a *P*-velocity jump of ~4 per cent assuming the PREM density model.

Key words: asthenosphere, array, mantle discontinuities, seismology, upper mantle.

1 INTRODUCTION

The layered structure of the upper mantle is mainly determined by seismic observations. The Earth's upper mantle is characterized by steep velocity gradients and by the existence of several discontinuous changes of velocity and density, called seismic discontinuities or for simplicity: discontinuities. The fine structure of the upper mantle discontinuities provides basic constraints on the chemistry, temperature and dynamics of the Earth's mantle.

Seismological techniques are especially suited to study these features, because seismic waves are reflected and converted at the discontinuities. Conversions from *P* to *S* waves at the upper mantle discontinuities (Vinnik 1977; Chevrot *et al.* 1999), receiver functions (Kind and Vinnik 1988), reflections of *PP* and *SS* waves from the discontinuities (Shearer 1991; Flanagan & Shearer 1998, 1999) and *ScS* reverberations (Revenaugh & Jordan 1991a–c) have been used to determine the depth, the velocity and density contrast and the sharpness of the discontinuities, i.e. the depth interval over which the seismic parameters change. Some discontinuities, e.g. the major discontinuities in the mantle transition zone at 410 km and 660 km depth, are globally observed with relatively little variation of the depth. These discontinuities are most likely correlated with phase changes in the pyrolite model of the mantle composition (Birch 1952; Ringwood 1975, 1991; Bina 1991). In some early refraction studies in Europe and North America, a reflector near 220 km depth was found (Lehmann 1959, 1961; Hales *et al.* 1980). The detection of this so called Lehmann discontinuity (the *L*) was confirmed later by surface wave studies (Goncz & Cleary 1976), underside reflections of depth phases from the discontinuity (Vidale & Benz 1992), *ScS* reverberations (Revenaugh & Jordan 1991b; Gaherty & Jordan 1995) and *P*→*S* conversions (Sacks *et al.* 1979). Most of these observations were made in continental regions with some isolated detections beneath island arcs. Despite numerous detections of this discontinuity its global existence is contentious. The reflector described here shows similar depths as the *L* and is perhaps the first detection of the *L* beneath a purely oceanic region.

Due to the lack of major solid–solid phase transitions at about 200 km depth (Bina & Wood 1984), different mechanisms for the origin of the *L* have been proposed. The interpretation

* Institute of Geophysics and Planetary Physics—Center of the Study of Imaging and Dynamics of the Earth, University of California, Santa Cruz, CA, 95064, USA
† Universität Potsdam, Institut für Geowissenschaften, D-14476 Golm, Germany

of the *L* as the sharp lower boundary of the astenospheric low velocity layer (LVZ) (Lehmann 1959, 1961) is unlikely because most detections of the *L* are beneath continental regions, where the LVZ is weak or absent.

A likely explanation for the *L* is a discontinuity resulting from lattice preferred orientation (LPO) of highly anisotropic olivine crystals in a deformation zone responsible for the mechanical decoupling of the lithosphere from the underlying mantle. This hypothesis is further discussed by Revenaugh & Jordan (1991b) and by Gaherty & Jordan (1995), and is generalized as a change in structure, from highly anisotropic lithosphere to an isotropic asthenosphere. This phenomenon of rapid decrease of anisotropy around a depth of $\sim$200 km is interpreted as the result of the pressure induced change of the deformation mechanism from dislocation creep to diffusion creep (Karato 1992). Such a change of anisotropy would cause a velocity jump for vertically, or almost vertically, travelling waves.

We study this upper mantle discontinuity using underside reflections of *PP* (P^dP, where *d* denotes the depth of the discontinuity where the energy is reflected). Short-period (1 Hz) array data and array methods are used, which allow us to enhance the signal to noise ratio (SNR) and to measure the vector velocity, i.e. backazimuth (Θ) and slowness (*u*), of the arriving phases with high resolution.

Besides the reflections from the L, the seismograms show P^dP from several different discontinuities like the 410 km discontinuity and at depths of $\sim$60–100 km in the upper mantle and the mantle transition zone. This manuscript focuses on the detection of the reflector at 200 km depth. Other results will be presented in the near future.

2 DATA

The data set used in this study consists of short-period (*sp*) recordings from the small aperture Yellowknife Array (YKA) located in the Northwest Territories of Canada. The array consists of 18 vertical *sp* stations in a cross shaped configuration. The location of YKA (triangle) (Fig. 1a) and its configuration (Fig. 1c) are displayed in Fig. 1. Each branch of the array is 20 km long with an interstation spacing of 2.5 km. The two branches are adjusted in N–S and E–W direction. The *sp* stations have a dominant period around 1 s. The array is particularly configured to detect weak, *sp P*-wave signals from different azimuths. Additional to the *sp* stations, four three-component broad-band stations located 10 km apart in the middle of the two branches exist, but are not used in this study.

In this study we use events originating from the western and south-western Pacific rim. The sources are near the North Island of New Zealand, Tonga, Fiji, Solomon, New Guinea and the Philippine Islands (Fig. 1).

We chose earthquakes from the YKA database based on the following criteria: (1) strong events with strong *PP* arrival with a SNR of *PP* to noise before the *P* onset better than 4 (in band-pass filtered data); (2) events with short *P* (or $P_{\rm diff}$) coda and (3) shallow events ($h \leq 100$ km) are preferred.

The *PP* reflections from the discontinuities are weak signals. However, strong events have enough seismic energy to raise the P^dP phases above the noise level. The onset of *PP* in short period data is difficult to detect. The exact measurement of the *PP* travel time is essential for a precise calculation of the reflector depth beneath the surface reflection point. Strong *PP* arrivals help to reduce these errors. The *P* coda must be decayed sufficiently before the *PP* precursors arrive, to avoid interference between *P* coda and P^dP. For the same reason, shallow events are preferred to avoid interference between the depth phases and P^dP. In total, 124 events from the appropriate source region recorded at YKA between September 1989 and March 1997 fulfill these criteria.

The source–receiver distance (Δ) for these events is 88°–116° with backazimuths of 232°–304°. These events are studied using the methods described below to detect P^dP. The location of all sources (stars), the reflection points (ellipses) and the location of YKA (triangle) are displayed in Fig. 1a. The reflection points fill a corridor from the Hawaiian Islands striking north-west. The Fresnel zone in Fig. 1 is represented as the centre of the actual saddle-shaped Fresnel zone. The isochrons for the min-max phase *PP* are displayed in Fig. 1b. This inner part of the Fresnel zone, defined by the ± 0.25 isochron (Berckhout 1984), is $\sim 4°$ along great circle path and $\sim 2°$ perpendicular to the great circle path. The fringes of the Fresnel zone extend to much greater distances and complicate the interpretation of the origin of *PP*.

3 METHOD

The P^dP phases have very small amplitudes. Hence, these phases cannot be observed in unprocessed, single seismograms. By using YKA data and applying different array techniques, it is possible to reduce noise and to identify P^dP. We use frequency-wavenumber analysis (fk-analysis) (Capon 1973) to identify the $P^{210}P$ phases. fk-analysis is a standard array technique which measures the power distributed among different slownesses and directions of approach (Aki & Richards 1980).

To detect P^dP phases in the recordings of a short-period small-aperture array, a reliable identification of these phases is necessary. In Fig. 2, a detail of a *P*-wave travel time panel computed using IASP91 (Kennett & Engdahl 1991) is shown. The travel times are aligned at 0 s on *PP*. The underside reflections from the discontinuities at depths of 410 km and 660 km are marked by $P^{410}P$ and $P^{660}P$. The discontinuity at 210 km is not included in IASP91, but its *PP* underside reflection travel time curve has been added. As can be seen from the parallel branches of *PP* and P^dP, the mother phase *PP* and the P^dP phases are characterized by a similar slowness ($u_{PP} - u_{P^dP} \leq 0.2$ s deg^{-1}). The *P* (or $P_{\rm diff}$) phase shows a slowness several s deg^{-1} smaller than *PP* and P^dP (2.4–3.3 s deg^{-1} smaller depending on distance). In the precursor time window up to 130 s before *PP*, not only the underside reflections P^dP, but also phases resulting from upperside reflections at the discontinuities ($Pp_{410}p$ and $Pp_{660}p$) arrive. Pp_dp is characterized by a slowness comparable to *P* (or $P_{\rm diff}$). Another group of phases arriving in the time window before *PP* are *P*-waves scattered or reflected in the Earth's crust and upper mantle (Cleary *et al.* 1975). It has been shown that early interpretations of precursors to *PP* as P^dP (Bolt *et al.* 1968; Wright & Muirhead 1969) are erroneous. The detected phases show slownesses too small to be interpreted as P^dP. These precursory arrivals were identified as $P_\Delta P$, a *P*-wave scattered at a distance Δ, for example $P_{20°}P$ represents a *P*-wave incident on the surface at an epicentral distance of 20° and there converted to scattered *P* (Cleary *et al.* 1975). These phases generally show lower or higher slownesses than *PP*, depending on the location of the scattering volume on the source or receiver side of the *PP* reflection point,

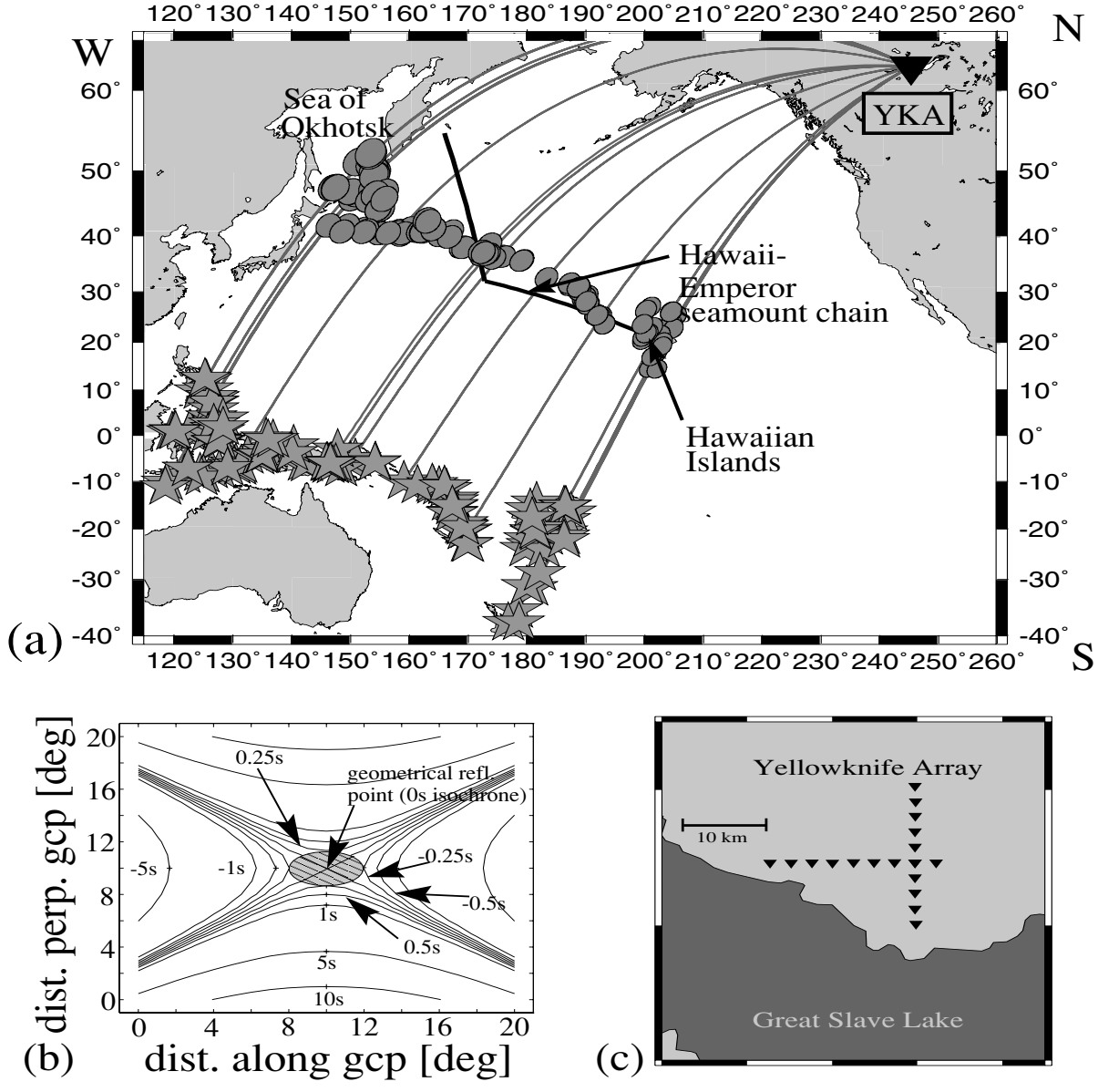

Figure 1. (a) The 124 sources used in this study are located at the western and south-western Pacific rim (stars), while the Yellowknife array (YKA) (solid triangle) is located in the Northwest Territories of Canada. The specific arrangement of the 18 vertical *sp* stations is shown in (c). YKA is located at Great Slave Lake. Every branch is ~20 km long and the interstation spacing is 2.5 km. Due to the source and receiver location, the surface reflection points (grey ellipses in a) fill a corridor from the tip of the Hawaiian Chain to the Sea of Okhotsk. The ellipses roughly represent the size of the 1 Hz Fresnel zone. The Hawaii-Emperor seamount chain is marked by the thick black line, while the thin black lines show the great circle paths between source and receiver. (b) Isochrons of *PP* for a distance of 100°. Along the x-axis, the distance along the great-circle path (gcp) is shown and on the y-axis, the distance perpendicular to the gcp. The ±0.25 s isochron represents the first Fresnel zone for 1 Hz data. The Fresnel zone is saddle shaped with fringes reaching out to large distances. The ellipses in Fig. 1a represent the central part of the Fresnel zone with an extent of 4° along great circle path and 2° perpendicular to the great circle path. (c) Station distribution of YKA. The stations are aligned in N-S and W-E directions. The aperture of the array is 20 km with an interstation spacing of 2.5 km.

respectively. For an example of scattered phases see Cleary *et al.* (1975) and for an example of a reflected phase see Weber & Wicks (1996). Such phases could also be generated off the great circle path and therefore show strong azimuthal deviations from the expected backazimuth. For the $P_{\Delta}P$ phases to arrive in the time window considered here, the reflection/scattering distance from the source or receiver would have to be approximately 20°–30°. Such phases, in turn, would have a slowness that is more than 2 s deg^{-1} smaller than the $P^{210}P$ phase studied here, or larger if the scattering occurs near the receiver.

Slowness and time, in combination with the backazimuth, are therefore reliable criteria to separate $P_{\Delta}P$ from the $P^{d}P$ phases discussed here. The three criteria to classify a precursor within the time window before *PP* as $P^{d}P$ are therefore:

(i) *Backazimuth*: the phase must travel along the great circle path between the source and receiver. This ensures that the phase was not reflected asymmetrically off the great circle-path, but that it travelled directly from source to receiver. The verification of the correct backazimuth therefore excludes

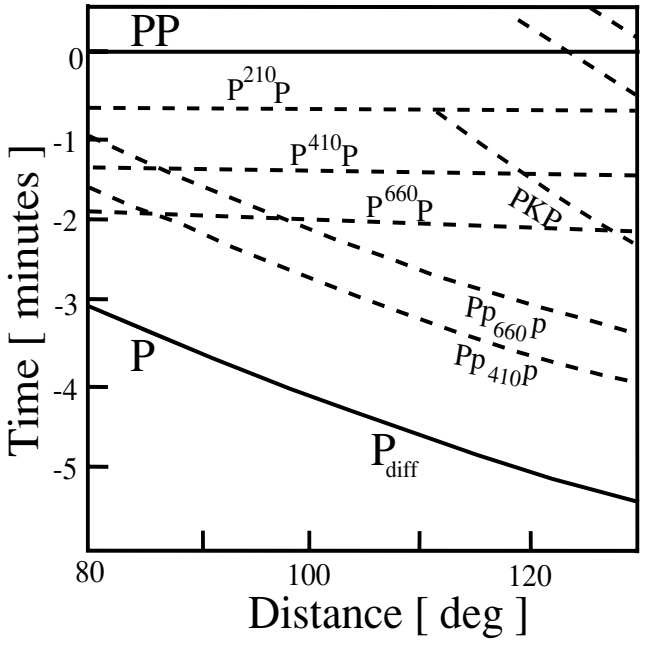

Figure 2. Travel time curves of *P* waves computed using model IASP91 (Kennett & Engdahl 1991) for distances of 80°–130°. The curves are aligned on the *PP* onset. Phases with the same slowness as *PP* (like the underside reflections P^dP) are parallel to *PP*, and these are marked by $P^{410}P$ and $P^{660}P$. Waves like *P* and the upperside reflections ($Pp_{410}p$ and $Pp_{660}p$) show a much smaller slowness. A discontinuity at a depth of 210 km is not part of IASP91, but the underside reflection from such a discontinuity ($P^{210}P$) is added for reference.

phases scattered/reflected from inhomogeneities off the great circle path. Additionally, coherent phases from other possible sources (second event within the time window or near receiver quarry blasts) can be identified and excluded.

(ii) *Slowness*: a slowness comparable to *PP* (at most 0.2 s deg^{-1} smaller than *PP*) indicates P^dP. The slowness of Pp_dp and $P_\Delta P$ is typically at least 2 s deg^{-1} smaller than that of *PP* and slowness can therefore be used to discriminate between these phases. Phases scattered on the receiver side of the *PP* reflection point, which show slownesses several s deg^{-1} higher than the *PP* slowness can also be identified via the slowness. Other phases, e.g. *PKiKP* for distances larger than $\sim$104°, might also arrive within the precursor time window, but they also show slownesses very different from those of *PP* (e.g. 1.8 s deg^{-1} for *PKiKP*).

(iii) *Coherency*: the coherency of the energy across the array is used to discriminate between (incoherent) noise and (coherent) phases arriving at the array. Noise might show, by chance, the right slowness and backazimuth to be interpreted as P^dP but is, as a statistical signal, not coherent. The resemblance of the fk-diagram (the output of the fk-analysis), to the array response function (ARF) can be used to interpret the coherency of the signal (Harjes & Henger 1973).

Backazimuth and slowness help also to focus on the central part (ellipse) of the saddle shaped Fresnel zone, since energy not contained in the ellipse given in Fig. 1 will have slownesses and backazimuths that deviate significantly from the values for energy reflected in the area of the ellipses. The difficulty of identification of P^dP without array processing is illustrated in Fig. 3. In Fig. 3a and b respectively, unfiltered and filtered seismograms of the YKA stations are shown. The filter used was a causal fourth-order Butterworth band-pass with cut-off frequencies of 0.5 Hz and 1.4 Hz. The arrivals of *P* and *PP* are marked. In the seismograms a small coherent phase 50 s before the *PP* arrival (marked by the question mark) is visible. An unambiguous identification as a *PP* precursor due to an underside reflection from an upper mantle discontinuity using only the seismograms is not possible because the conformity of the slowness and backazimuth of the precursor phase with *PP* is not obvious.

Fig. 4a–e shows beam traces of all 124 events of the data set. The beam traces are calculated using the theoretical *PP* slowness and backazimuth. The events are grouped with respect to the location of the *PP* surface reflection points. A map of the distinct regions of the study area is shown in Fig. 4f. The beam traces are aligned on the $P(P_{\rm diff})$ onset due to the easier identification of the onset and normalized with respect to the *PP* amplitude. The arrival times of $P(P_{\rm diff})$, *PKiKP* and *PP* are indicated.

The beam traces show a decay of beam energy in the *P* coda after the *P* onset. Within the relatively quiet time window before the *PP* onset several onsets are visible. This is the time window where the P^dP phases are expected. Some possible *PP* precursors which may originate from the *L* are marked by arrows. These phases arrive in a time window appropriate for an identification as $P^{210}P$ with some variation of the reflector depth. Not all of the wavelets in the time window before *PP* can be attributed to *PP* underside reflections from upper mantle discontinuities, but to scattered energy and upperside reflections as discussed above. The distinction is possible by a careful study of the slowness and backazimuth of the precursors using the fk-analysis. The beam traces have no good control of slowness and backazimuth.

A better control of the slowness of a phase can be obtained with 4th-root vespagrams (Muirhead & Datt 1976; McFadden *et al.* 1986) (Fig. 5). Figs 5a-c show events with detected $P^{210}P$ (events 7, 11, 14 in Table 1) and Figs 5d–f show events without detected $P^{210}P$. The higher slowness of the $P^{210}P$ phases in comparison with other phases in this time window is obvious. No other phases in the time window appropriate for the upper mantle discontinuities show the high slowness we demand as one parameter to identify a phase as P^dP. Fig. 5c shows that many phases can arrive as precursory phases to *PP*, but due to the slowness comparable to *P* these phases are upperside reflections off the discontinuities or scattered energy (Cleary *et al.* 1975). The 4th-root vespagrams are calculated using a fixed backazimuth, in our case we use the theoretical backazimuth between receiver and source. Therefore, the 4th-root vespagrams cannot be used to measure the backazimuth of the *PP* precursors. Using a wrong backazimuth while calculating the 4th-root vespagrams results in wrong slownesses of the phases which travel along a deviating backazimuth (Rost & Thomas 2001).

Due to the necessity to control slowness, backazimuth and coherency of the precursory phases, the criteria as discussed above were tested using the fk-analysis. The first two criteria are hard criteria, that is, a possible P^dP phase must show a similar slowness and backazimuth to *PP* within the resolution of the fk-analysis. The third criterion is more qualitative and the correspondence between the fk-diagram and the ARF is examined visually. Phases showing different slownesses, and/or backazimuths and/or incoherent signals can therefore be excluded from the list of P^dP arrivals.

Table 1. Events showing a reflector between 150 and 250 km depth. The following parameters are given: # event number, origin date, time, event latitude, event longitude, source depth, magnitude (m_b), distance (Δ), backazimuth (Θ), depth (d), estimated depth error Δd. The event locations are from Engdahl *et al.* (1998). d denotes the depth of the reflector computed with model IASP91 and Δd is the estimated error of the depth location.

#	Origin	time	lat (deg)	lon (deg)	Depth (km)	m_b	Δ (deg)	Θ (deg)	d (km)	Δd (km)
1	1989 Dec 07	13:38	−6.48	146.43	115	6.1	99.9	275.0	166	8
2	1989 Dec 09	20:38	0.18	123.46	154	6.3	104.1	299.0	230	9
3	1990 Apr 18	13:39	1.16	122.64	28	6.2	103.4	300.0	211	8
4	1991 May 19	00:58	1.16	122.96	31	6.0	103.4	299.9	212	8
5	1991 May 31	05:28	−6.05	130.60	85	6.0	106.6	289.6	229	8
6	1991 Jun 07	11:51	−7.20	122.53	536	6.2	111.1	196.7	225	8
7	1991 Jun 20	06:27	1.17	122.88	21	5.6	103.4	299.9	198	8
8	1992 Mar 04	03:49	−3.01	147.88	19	6.0	96.1	275.3	216	8
9	1992 Aug 09	19:49	4.02	126.51	68	6.1	99.3	297.7	210	8
10	1993 May 11	18:26	7.22	126.57	59	6.1	96.4	299.0	200	10
11	1993 Jun 04	10:49	3.73	128.50	20	5.9	98.8	295.8	210	8
12	1993 Aug 20	05:06	−6.00	142.74	15	6.0	101.1	278.5	163	10
13	1993 Oct 16	03:05	−5.90	146.20	27	6.2	99.5	275.4	212	8
14	1994 Jan 19	01:53	−3.18	135.97	23	6.1	101.7	285.9	171	10
15	1994 Feb 12	17:58	−20.50	169.36	28	6.4	101.8	248.3	194	8
16	1994 May 25	04:03	−4.30	135.49	2	6.0	102.8	285.9	212	9
17	1994 Oct 08	21:44	−1.26	127.98	17	6.4	103.5	294.1	209	9
18	1995 Jan 21	07:30	1.56	126.88	42	6.2	100.5	296.8	195	12
19	1995 Apr 21	00:09	12.01	125.66	20	6.9	92.42	301.8	215	8
20	1995 May 16	20:12	−23.01	169.90	20	6.9	103.7	246.7	212	9
21	1995 May 29	07:29	−10.25	164.00	26	6.4	95.1	257.7	175	8
22	1995 Sep 22	05:39	−6.05	146.54	45	6.0	109.5	296.0	198	8
23	1996 Feb 17	14:21	−0.57	135.84	19	6.5	99.5	287.2	200	9
24	1996 Feb 17	20:18	−0.92	136.23	32	6.6	99.6	186.7	181	10

The original fk-analysis is restricted to short time windows and cannot be applied to the entire length of a seismogram. To study the development of slowness and backazimuth over a period of time in the seismograms, a sliding-window fk-analysis has been developed and is used for the study of P^dP phases. As an additional advantage, sliding-window fk-analysis allows the search of P^dP phases in numerous time windows, and not only in time windows where the underside reflections from known discontinuities are expected.

For the sliding-window fk-analysis a short time window of constant width is shifted along the seismogram with a constant step size, and a standard fk-analysis is performed for every time window. The results of the fk-analysis, i.e. the slowness and backazimuth of the power maximum and the information on the coherency of the signal for each time window, are stored. Strictly speaking the sliding-window fk-analysis transfers the seismogram into a coherency time series with respect to slowness and backazimuth.

To obtain the best possible results in the fk-analysis, a suitable time window and step size must be chosen. The time window must be wide enough to completely include all phases travelling over the array with different slownesses. In shorter time windows, not all components of the signal can be analysed and the fk-analysis becomes less accurate. Windows which are too large contain more noise, which disturbs the exact determination of slowness and backazimuth. In particular, the coherency of the signal decays and the time resolution of the method decreases. The window width is defined by the dominant period of the signal and its travel time over the array. This travel time depends on the slowness of the studied phase.

For YKA data a window width of 4 s and a step size of 1 s is used to detect the P^dP phases. Therefore, every second of the seismogram is sampled by four different time windows.

The results of the fk-analysis are displayed as a frequency-wavenumber power spectral density as a function of slowness and backazimuth. The power spectral density is plotted in a polar coordinate system called the fk-diagram with the backazimuth on the azimuthal axis and the slowness on the radial axis. Some snapshot examples of the sliding-window fk-analysis are shown in Fig. 6. The maximum energy is set to 0 dB and the lines mark −1 dB power isolines. A colourscale valid for all fk-diagrams is shown on the right hand side of Fig. 6. For the sliding-window fk-analysis the fk-diagrams of all time windows are normalized to the maximum of all fk-diagrams of the seismograms.

Fig. 6a shows one trace of a synthetic signal recorded at a station of an array with YKA configuration. This shows that the signals, buried in white noise added to the trace, cannot be identified in a single trace. 11 damped sine signals with signal lengths of 2 s and varying amplitudes are contained in this trace. The amplitudes are smaller than the noise amplitudes; therefore, the individual signals are not visible. The synthetic signals arrive with a slowness of 7.75 s deg^{-1} and along a backazimuth of 225°. The amplitudes of the signals are varied and the time windows of the signals are marked by the vertical boxes. In Fig. 6b the synthetic signal and the white noise have the same amplitude ($A_{signal}/A_{noise} = 1 = 100$ per cent). The slowness and backazimuth are correctly resolved by the fk-analysis. The signal amplitude is decreased for the following signals. In this resolution test the fk-analysis can resolve signals with only

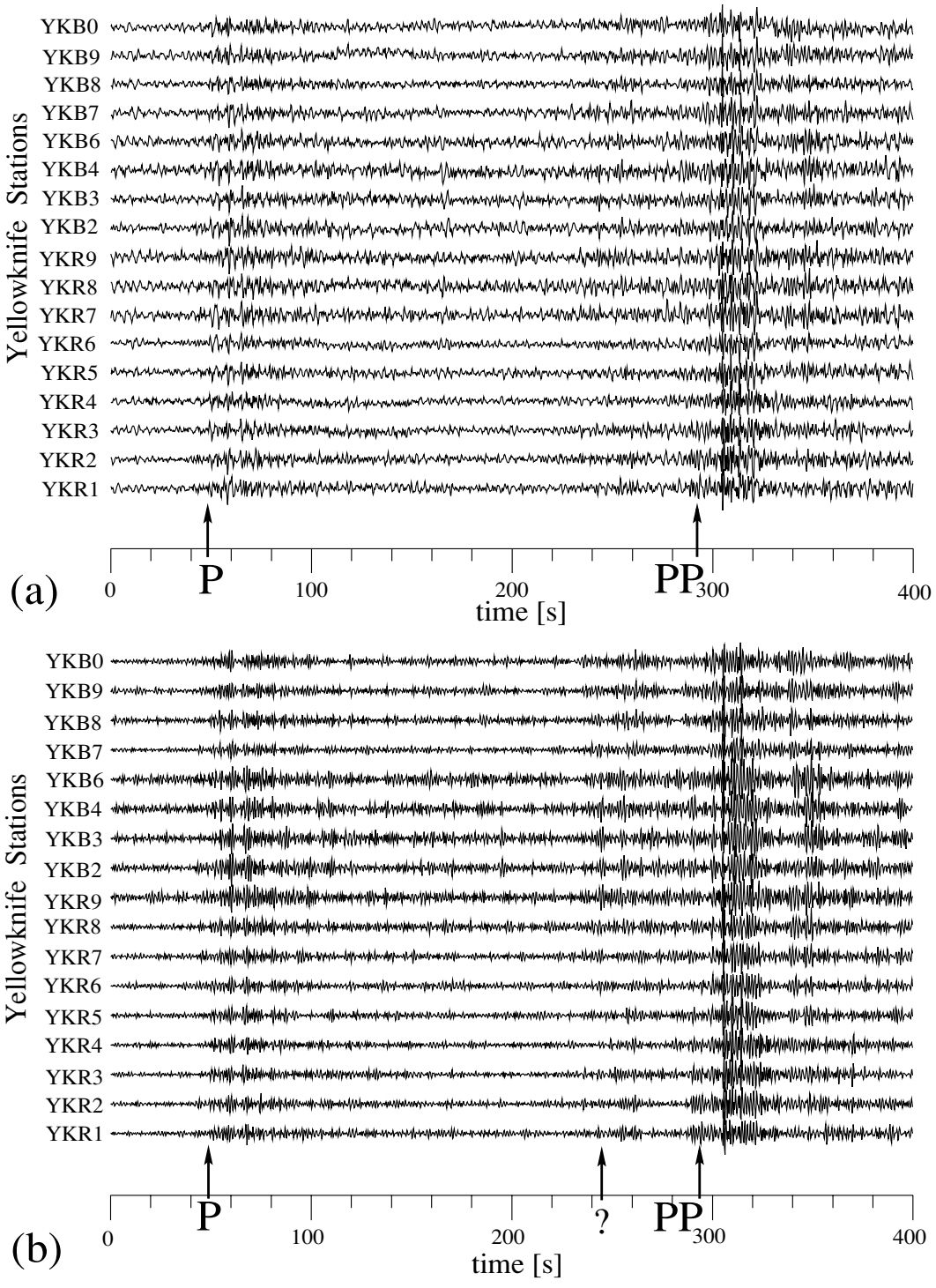

Figure 3. (a) Unfiltered seismograms of all available YKA stations. Event 17 (Table 1) is displayed having a distance $\Delta = 103.5^\circ$, a backazimuth of 294.1° and a depth $h = 17$ km. The *P* and *PP* onset are marked by arrows. A weak phase ~ 50 s before *PP* is visible (indicated by the question mark). (b) Bandpass filtered version of (a). A causal fourth-order bandpass with cut off frequencies of 0.5 and 1.4 Hz was applied. This filter was chosen to reduce the noise on the traces and to enhance the amplitudes of the coherent phases. Again the *PP* and *P* travel times are marked. The weak phase ~ 50 s before *PP* is now better visible (indicated by the question mark).

40–50 per cent of the noise amplitude (Fig. 6e and f). The assumptions of white noise and a 2 s long sine signal are artificial. Natural noise and seismic signals show different spectra compared to the synthetic signals used in the resolution test. Inhomogeneities along the ray paths to different array stations are the reason that the real signals arriving at the array are not as perfectly coherent as assumed in the synthetic tests. Nevertheless, this resolution test gives estimates on the maximum resolution of the sliding-window fk-analysis. A detection limit of ~ 50–70 per cent is used for further interpretation of the results.

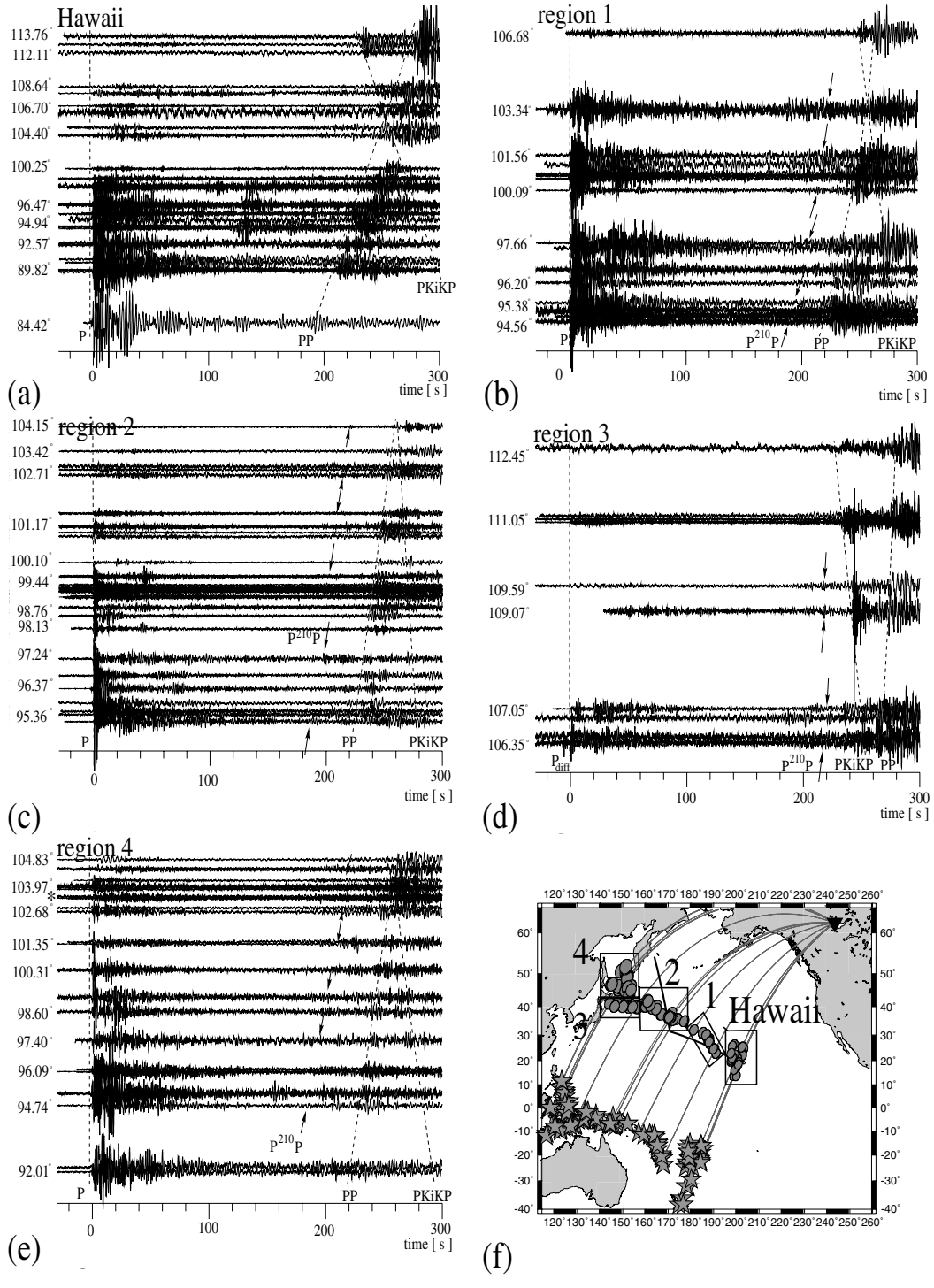

Figure 4. Beam traces of all 124 events of the data set. Beams were calculated with *PP* slowness and backazimuth. The beams are aligned on the *P* onset and are shown in distance dependent plots, with distances given on the left. The events are grouped in 5 regions as (a–e). A map of the location of the 5 regions is given (f). Possible precursors to *PP* originating from the *L* are marked by the arrows. The event shown in Fig. 3 is marked by a star in region 4.

The advantage of the sliding-window fk-analysis can best be seen in so-called, fk-movies, where all fk-diagrams are displayed in an animated movie (Rost 2000). Examples of these movies are shown in Rost (2000) or can be studied at http://www.uni-geophys.gwdg.de/˜srost/fk-movies.htm.

The sliding-window fk-analysis was applied to all 124 events of our data set. The complete time window from ∼10 s before *P* to ∼30 s after *PP* was studied and without any focus on certain time windows all phases satisfying the criteria discussed above were marked. These precursors in the data set were not randomly distributed in the whole time window, but could be grouped in three intervals with respect to their reflector depth. Corresponding reflector depths of ∼410, ∼200 and ∼60–100 km were found. This manuscript describes the reflections from

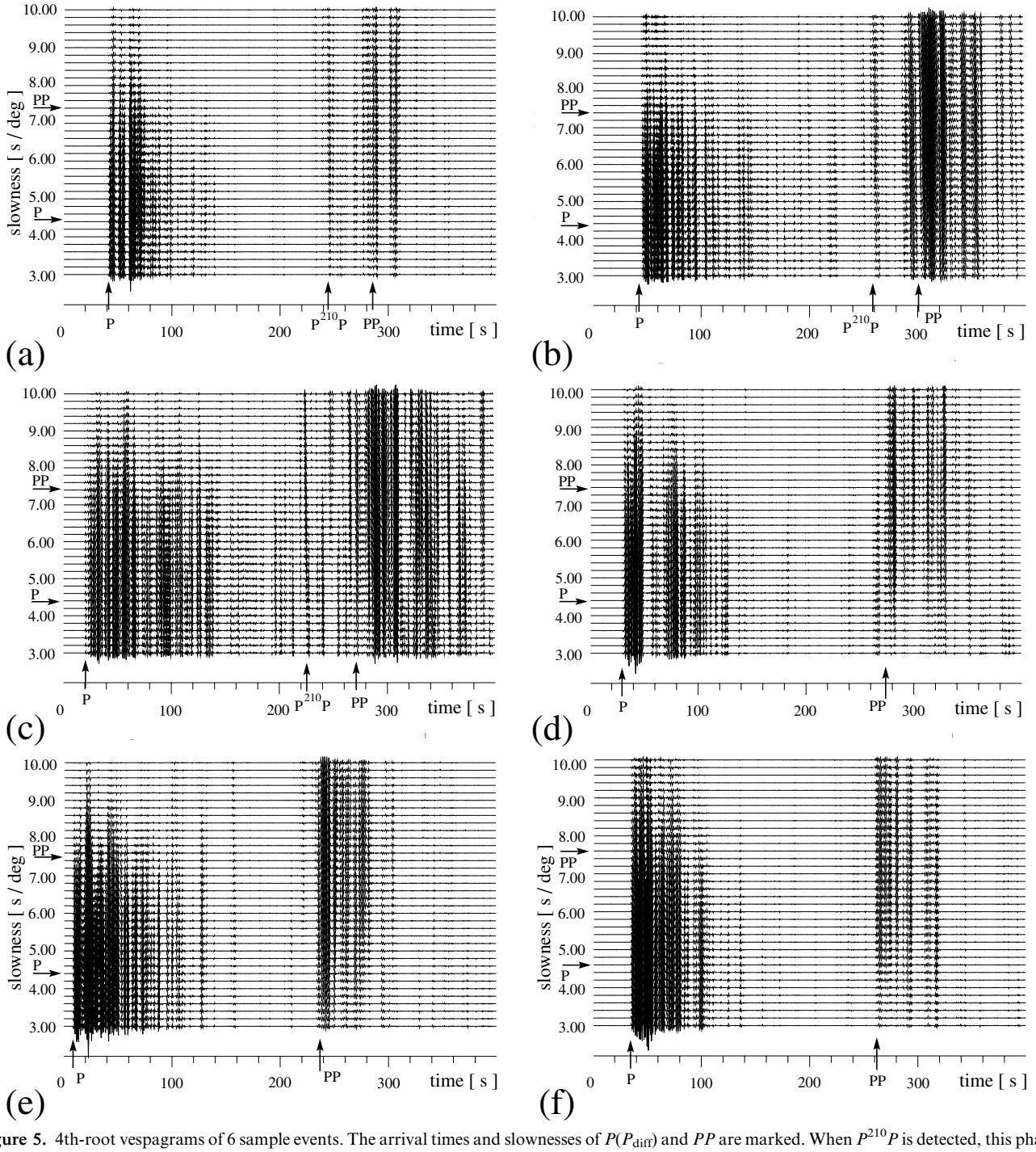

Figure 5. 4th-root vespagrams of 6 sample events. The arrival times and slownesses of $P(P_{diff})$ and PP are marked. When $P^{210}P$ is detected, this phase is also marked . (a) 1993 June 4 (event 11 in Table), (b) 1994 January 19 (event 14), (c) 1991 June 20 (event 7), (d) 1992 October 11 (h = 135 km, $\Delta = 100.63°$, $\Theta = 248.9°$) , (e) 1994 April 27 (h = 33 km, $\Delta = 95.62°$, $\Theta = 233.0°$) (f) 1995 May 29 (h = 21 km, $\Delta = 95.04°$, $\Theta = 257.2°$).

~200 km depth, whereas the others are described elsewhere (Rost & Weber 2001). The time intervals between these groups do not show precursors which could be identified according to slowness, azimuth and wave coherency as P^dP.

The application of the sliding-window fk-analysis on real data (event 17) can be seen as snapshots in Fig. 7. The beam trace together with the colour scale for the fk-diagrams is shown in the middle of the figure for orientation. The arrival times for P, PP and $P^{210}P$ are marked by blue lines, while the snapshot time windows studied by the fk-analysis are marked by boxes. The snapshots of the sliding-window fk-analysis are shown in Figs 7a–d. The theoretical values for u and Θ are marked by the white diamonds and the maximum of the fk-analysis is marked by a circle. The slowness difference of ~3.25 s deg^{-1} between P and PP in Fig. 7a and Fig.7b is obvious. The fk-diagrams closely resemble the cross shaped form of the array response function (ARF) of YKA. Both phases are highly coherent. For comparison a time window without a coherent phase is shown in Fig. 7c. The signal amplitude is low, as indicated by the yellow and blue colours, and

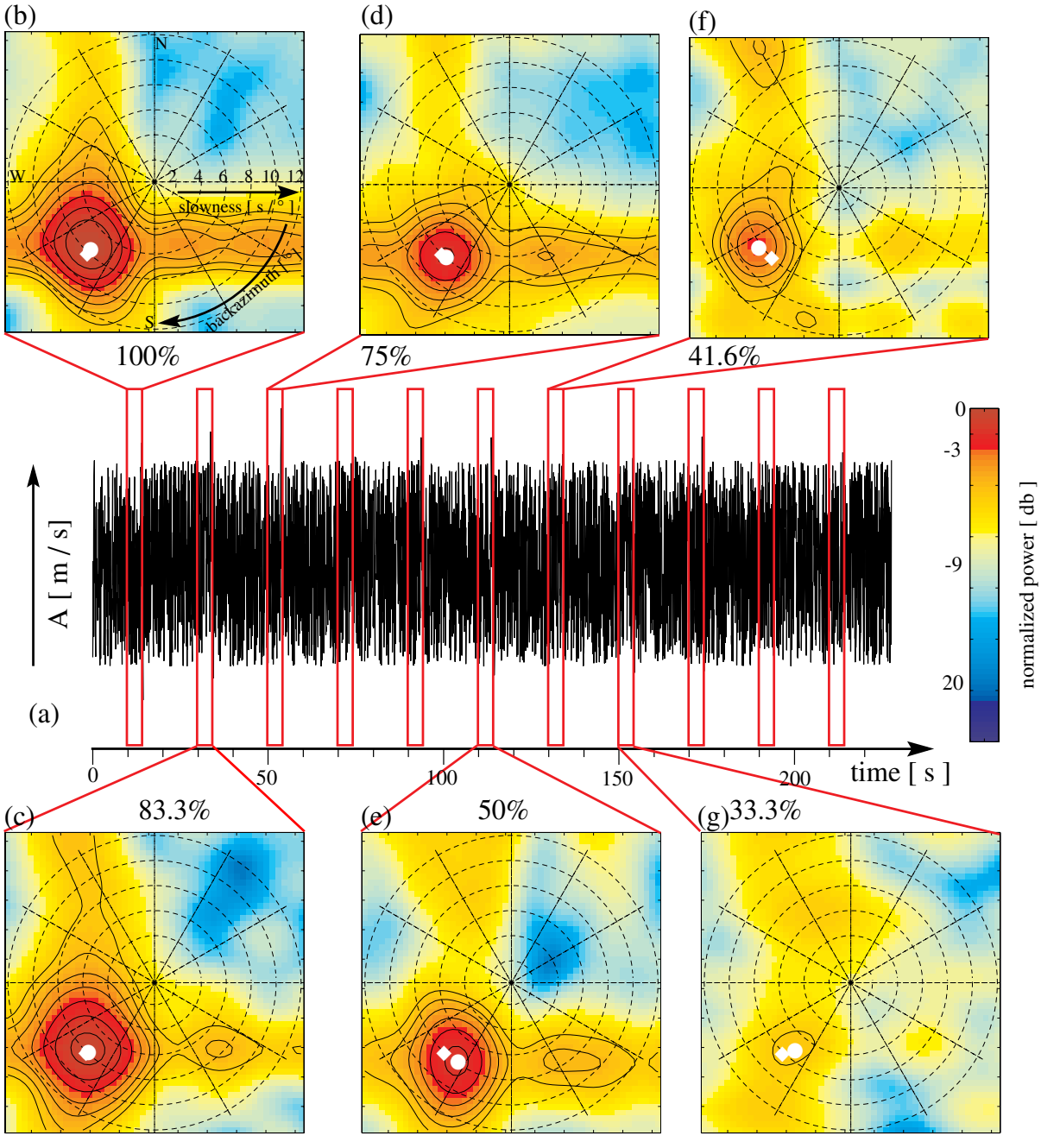

Figure 6. Examples of frequency-wavenumber diagrams (fk-diagrams) and noise resolution tests for the fk-analysis. White noise is added to a synthetic signal recorded at an array with YKA configuration. The signals arrive as a coherent wave with a slowness of 7.75 s deg^{-1} and a backazimuth of 225° at the array. 11 tapered sinusoidal signals with signal lengths of 2 s and varying amplitudes are included in the seismograms. (a) Seismogram of one array station. The travel times of the 11 signals, which are buried by the noise, are marked by the boxes. Six fk-diagrams for different time windows are displayed in (b)–(g). (b) fk-diagram of a phase with a ratio of signal to noise amplitude of 1. The azimuthal axis shows the backazimuth Θ (in °) and the radial axis shows the slowness u (in s/°). The colour represents logarithmic energy with the maximum of 0 dB (red) and the minimum (≤ -20 dB) in blue. The lines mark -1 dB isolines. The maximum of the fk-diagram is marked by the white dot and the theoretical slowness and backazimuth value for the incident phase is marked by the white diamond. The slowness and backazimuth of the wave is well resolved and the coherency of the signal is very good. (c) Signal amplitude 83.3 per cent. Good u and Θ determination. Coherent signal. (d) Signal amplitude 75 per cent. Good u and Θ determination. Coherent signal. (e) Signal amplitude 50 per cent. Small slowness and backazimuth deviations. (f) Signal amplitude 41.6 per cent. The signal can still be identified as a coherent signal arriving with the defined slowness and backazimuth. (g) Signal amplitude 33.3 per cent. No signal detectable.

the cross shaped form of the ARF cannot be identified. The time window with a $P^{210}P$ phase is shown in Fig. 7d. The phase travels along the great circle path and shows the high slowness of PP. The comparison with Fig. 7b shows the coherency of the signal.

To measure the depth of the reflector where the PP phase is reflected, the differential travel time $\Delta T = t_{PP} - t_{P^{210}P}$ is used. The depth is computed from ΔT using ray tracing methods and the Earth model IASP91 (Kennett & Engdahl 1991). Neele *et al.*

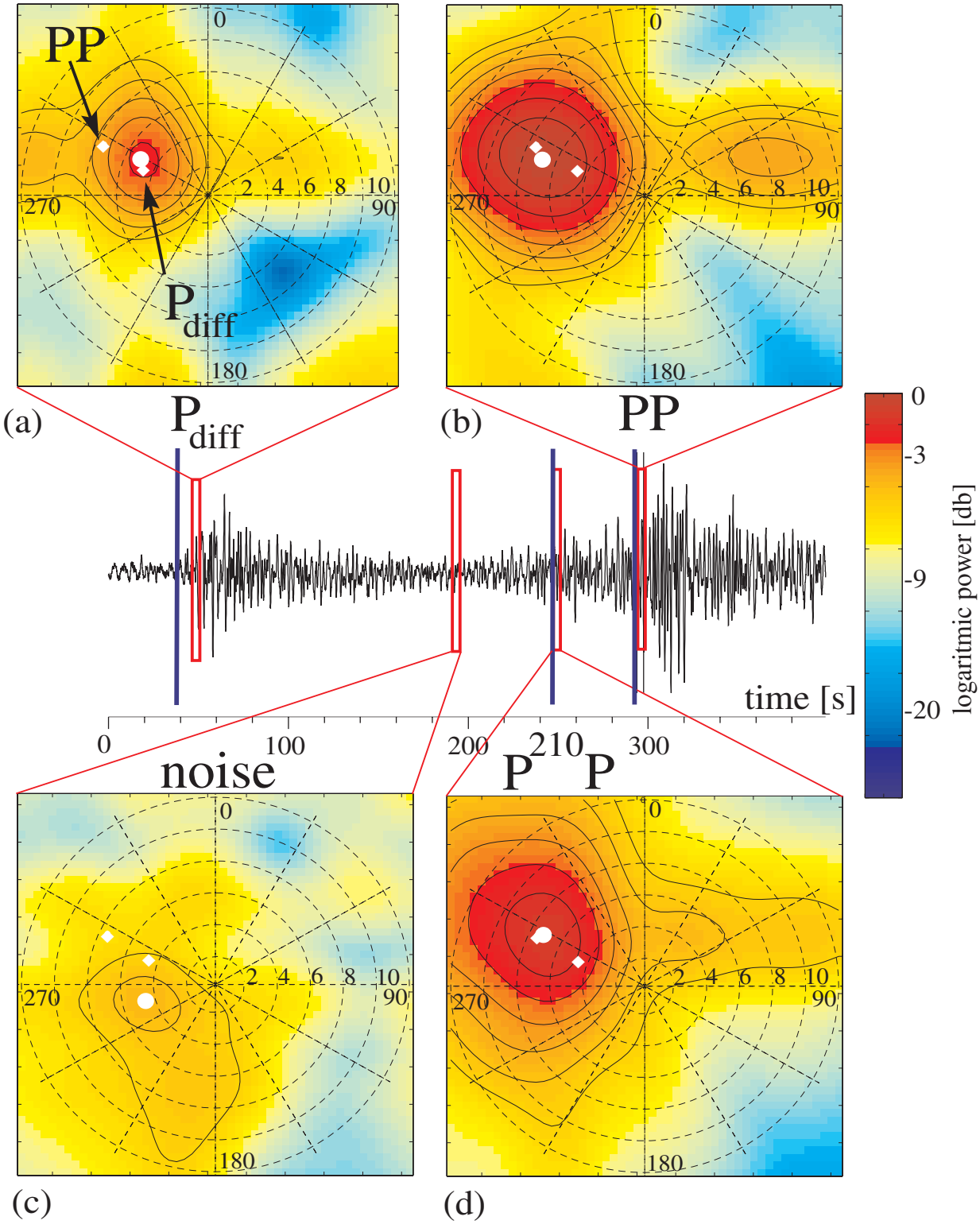

Figure 7. Snapshots of sliding-window fk-analysis for event 17. The centre of the figure shows the beam trace of the seismograms recorded at YKA. The beam trace was computed with the theoretical Θ and *PP* slowness to enhance the amplitudes of *PP* and its precursors in the seismogram. The beam trace is displayed to show the locations of the selected time windows shown above and below. The colour scale for the normalized power for the fk-diagrams is given. (a) fk-diagram of the P_{diff} time window. The theoretical Θ and u of P_{diff} and *PP* are marked by the white diamonds, respectively with the low slowness marking $u_{P\mathrm{diff}}$ (4.5 s/°) and the higher slowness u_{PP} (7.5 s/°). The maximum energy of the fk-diagram is marked by the white dot. The lines show logarithmic −1 dB energy isolines and the energy maximum is set to 0 dB. (b) fk-diagram of *PP* (Note the high slowness). (c) fk-diagram of noise window. The energy is (incoherent) scattered energy of the *P*-coda. (d) fk-diagram of $P^{210}P$ characterized by the similar slowness relative to *PP*. The phase is coherent as can be seen by the resemblance to the array response function.

(1997) suggested that short wavelength topography on the discontinuity could cause significant errors in the estimates of discontinuity depth, but this effect should not bias the topography measured using short-period data significantly. The midpoint of the 4 s fk-analysis is used as a reference for the computation of the differential travel time.

From the 124 events analysed here, 24 events show P^dP with reflector depths d ranging from $\sim$160 to $\sim$230 km. These events are listed in Table 1, where the origin time, the source parameters (latitude, longitude, depth and magnitude), distance (Δ) and backazimuth (Θ) to YKA are given. The origin times and source locations are those determined by Engdahl *et al.* (1998).

For simplicity all precursors from this depth range are called $P^{210}P$ in the following. The column d gives the apparent depth of the reflector, assuming the IASP91 velocity structure. The column Δd gives the estimated error of the depth location. The apparent discontinuity depths depend upon the velocity in the upper mantle above the discontinuities; that is, slower velocities relative to the reference model would result in greater apparent depth. Thus, lateral heterogeneity in the upper mantle will introduce errors into the computed discontinuity depths. The surface reflection points are located in regions where the lithosphere is older than 110 Ma (Müller *et al.* 1997) and, according to Woodward & Masters (1991), the *PP–P* differential travel time residuals for old oceanic lithosphere (age $\geq$100 Ma) are smaller than 1 s. Hence, the error due to lateral heterogeneity in the upper mantle is most likely small. The picking error of $P^{210}P$ is 1 s due to the small signal amplitude. The *PP* picking error is $\sim$1 s due to the emergent *PP* onset. The total time error can therefore be estimated to be $\pm$2 s. These time errors define the depth error of approximately $\pm$8 km listed as Δd in Table 1.

Fig. 8 shows the measured depths of the reflector for all events showing $P^{210}P$. The depths of the reflection points are shown as column heights and are additionally coded in grey scales, the columns being located at the position of the geometrical *PP* reflection point. The solid line marks the strike of the Hawaii–Emperor seamount chain and the dashed line shows the strike of the depth profile shown in Fig. 9. The mean depth of all reflections is 200 km, as indicated by the solid line in Fig. 9, with an error of $\pm$20 km. The depth distribution of the reflection points indicates strong depth variation and steep topography of the reflector. This is in disagreement with previous studies of the Lehmann discontinuity and will be discussed in the next section.

Different reasons for the large number of events not showing reflections from the Lehmann discontinuity exist. First, the small amplitude P^dP phases can be overprinted by other phases as Pp_dp, $P_\Delta P$ or *PKiKP* (for Δ larger $\sim$112°) making an unambiguous identification of $P^{210}P$ difficult. When several phases with different slownesses and backazimuths arrive simultaneously at the array, the fk-analysis measures either a mean slowness and backazimuth, when the phases have similar amplitudes, or the slowness and backazimuth of the stronger phase, when the amplitudes are seriously different (Rost 2000). Additionally, the topography of the reflector is the source for focusing and defocusing effects which can be the reason for the discontinuous detection of the reflector.

Some reflection points are suited to study the influence of the subducted slab at the Kuriles subduction zone on the *L* (Fig. 10). The depth of the reflector is given at the location of the geometrical reflection point and shaded in grey. Only a few points sample the area where the slab intersects the L. No depth variation correlated with this possible intersection is visible, indicating that the *L* is most likely not formed by a temperature controlled mechanism.

4 DISCUSSION

The detection of a reflector near 200 km depth is the first evidence for the Lehmann discontinuity beneath oceanic regions. The detections of the *L* using *ScS* reverberations in the region between Tonga–Fiji and Hawaii (Gaherty *et al.* 1999) have to

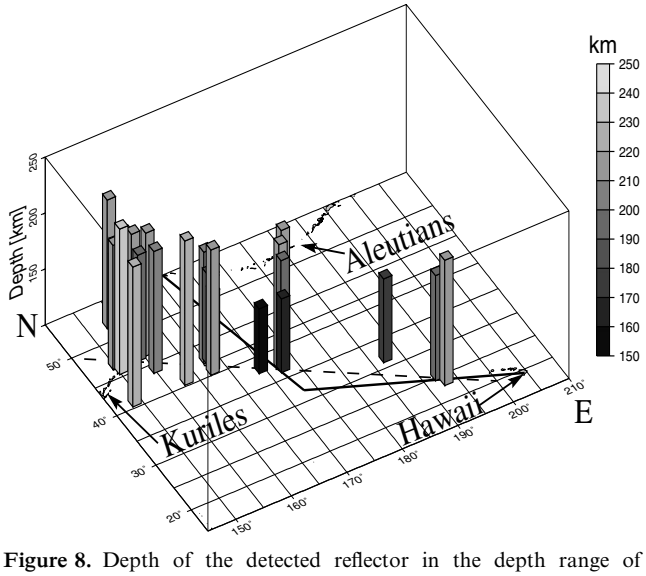

Figure 8. Depth of the detected reflector in the depth range of 150–250 km. The depth is shown as column height and is additionally coded as grey scale. The columns are located at the geometrical reflection point of *PP*. The thick solid line marks the Hawaii–Emperor seamount chain, while the dashed lines indicate the strike of the depth profile shown in Fig. 9.

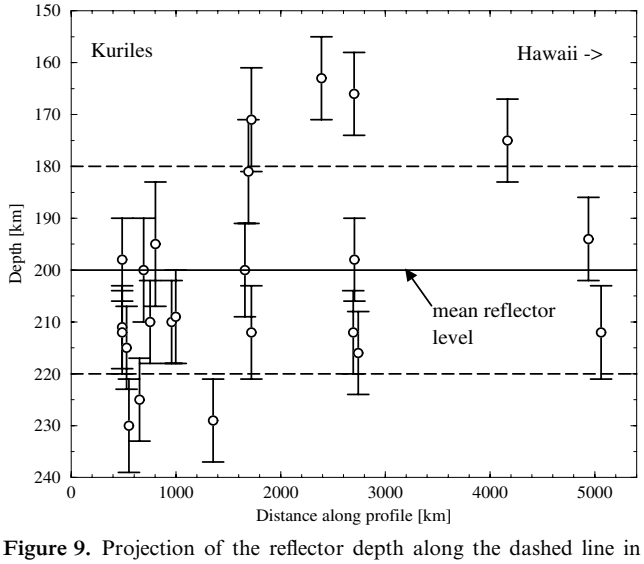

Figure 9. Projection of the reflector depth along the dashed line in Fig. 6. The depth error bars are as listed in Table 1. The mean of all depth values is 200 km (solid line) with a standard deviation of 20 km (dashed lines).

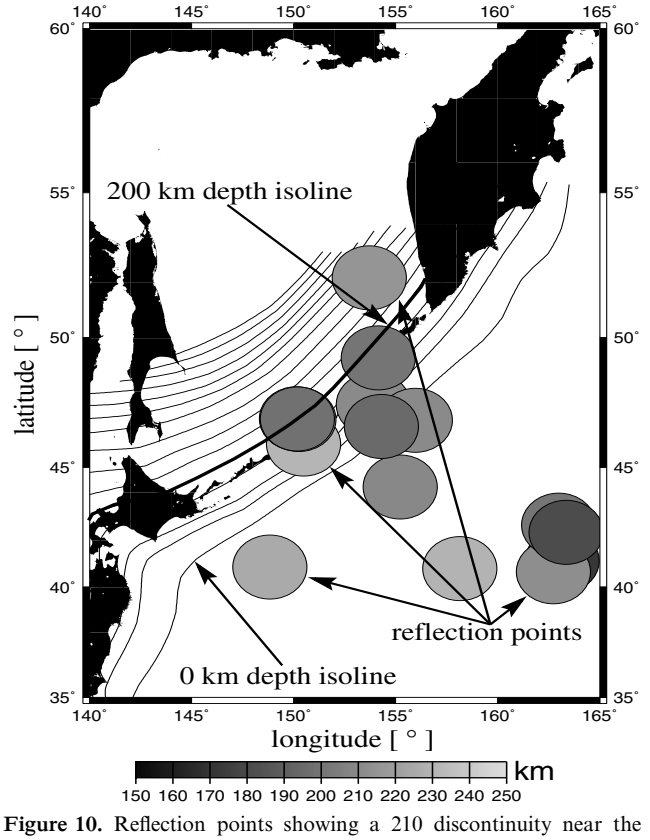

Figure 10. Reflection points showing a 210 discontinuity near the Kuril subduction zone. The depth of the reflector is coded in gray scales. The size of the circles indicates the inner part of the first Fresnel zone. The thin lines mark depth isolines of the subducting slabs plotted at 50 km intervals (Gudmundsson & Sambridge 1998). The 200 km depth isoline is marked as a thick line.

be treated with care, because the impedance contrast is close to the minimum resolution and is probably a result of the limited modelling parametrization used (Gaherty *et al.* 1999). Previous detections in oceanic regions using precursors to *pP* were located in the vicinity of subduction zones (Vidale & Benz 1992). The lack of occurrence of the *L* in oceanic regions is most likely a result of a lack of data, because most studies reporting the *L* used seismic refraction data or methods studying the structure of the upper mantle discontinuities near the source or the receiver. The use of *PP* precursors offers an ideal tool to study areas not covered by stations or earthquakes.

In previous studies, the depth of the *L* varied strongly for different tectonic regions, but the mean depth of the *L* in this study (h = 200 km) is in good agreement with the value of 211 km derived by Vidale & Benz (1992). The reflector depth in this study shows variations larger than the estimated depth error of ~8 km even within the first Fresnel zone, an effect observed even for events that sample the same region. The similarity of the great circle paths excludes lateral velocity heterogeneities along the path as a possible reason for the different apparent depths. Although the sources of events with similar great circle paths are located in a small region, the strong heterogeneity of the slab could generate travel time disturbances of 1–2 s (Weber 1990). These travel time disturbances could produce a depth error of ~10 km for the depth of the reflector. Furthermore, the Fresnel zone is the projection of the Fresnel volume on a horizontal plane. The influence of small undulations of reflector depth on the structure of the Fresnel zone at 1 Hz, as necessary for the data used here, has not been studied yet, but might become possible in the future with the advent of even more powerful computers. These aspects complicate the interpretation of the small scale variations of the reflector depth.

The strong depth variation of the *L* is unexpected. The reflections shown in this study cannot be used to prove the existence of a continuous discontinuity at ~200 km depth. The different depths of the reflector could also indicate a layer of normal mantle material with embedded heterogeneities. The scale of the heterogeneous bodies must be several wavelengths of the short-period waves, but smaller than the wavelengths for periods of 15–20 s used in long-period studies. Larger heterogeneities would produce reflections also in long-period data, which are not observed. This estimate indicates scale lengths of less than 20 km for the heterogeneities. The detected $P^{210}P$ signals sometimes show very large amplitudes. Either the local impedance contrast of the heterogeneities is large, or constructive interference of the different reflections at the isolated bodies generates the large amplitudes.

If the results in Fig. 9 are taken at face value, the topography indicated by the scattered depth reflections is very steep. Depth variations of ~40 km on scalelengths of 4° can hardly be explained by temperature variations; therefore a temperature induced mechanism for the *L* is, in our opinion, not supported by the observations (comp. also Fig. 10). The small-scale topography could explain the lack of a 210 km discontinuity in long-period studies as stacks of recordings with adjacent reflection points would not stack coherently. Underside reflections from the upper mantle discontinuities are very sensitive to the presence of topography on the discontinuity (Davis *et al.* 1989; Chaljub & Tarantola 1997; Neele & deRegt 1999). The topography breaks the symmetry of the ray-paths of the underside reflections and as a result the wavefield is focused or defocused at the receiver. The 3-D small-scale structures inferred from the study of high frequency waves can, at present, not be modelled with synthetic seismograms. Nonetheless, previous results using longer wavelengths show that focusing effects depend strongly on the curvature of the topography (Davis *et al.* 1989; Chaljub & Tarantola 1997). The steep topography detected on the *L* should therefore produce strong focusing and defocusing of the wavefield.

Comparing the results of long-period *PP* underside reflections with the outcome of this study, the lack of the *L* in the long-period studies (e.g. Shearer 1991) is striking, because the *L* produces such strong onsets in our data (see Figs 3 and 5). Besides the topography on the reflector, which can destroy the coherent stack of the precursors in data sets covering large regions, a lamination of the reflector could result in a reduced long-period signature (Vidale & Benz, 1992). This hypothesis is tested using synthetic seismograms. Fig. 11a shows synthetic seismograms calculated with the reflectivity method (Müller 1985) for different laminated models of the Lehmann discontinuity. The thickness *h* and the distance *d* between the lamellae was varied (Fig. 11b). The models consist of 4–6 layers with a 1 per cent velocity (v_P) and density increase, while the *S*-wave velocity structure was not changed. All seismograms except the first one at the top have a dominant period of 1 s. The long-period ($T_{\mathrm{dom}} = 15$ s) seismogram shown as top trace in Fig. 11 does not show a dominant signal from a layered stack of discontinuities with a thickness and a distance of 4 km. The different models tested for the 1 Hz data indicate that a layer

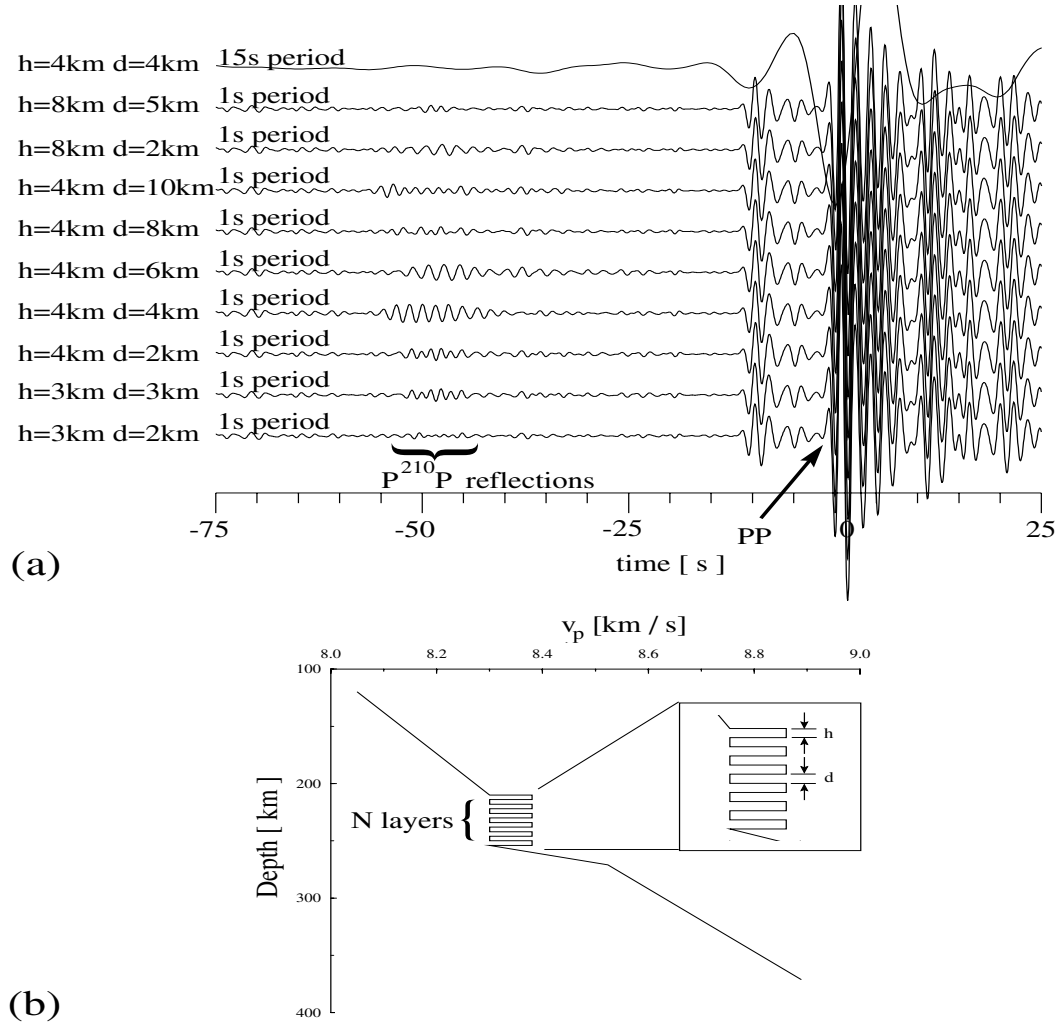

Figure 11. (a) Synthetic seismograms computed for laminated models of the Lehmann discontinuity. The thickness h and the distance d (see part b of this figure) between the single lamellae were varied. Most seismograms were computed with a dominant period of 1 s. The top trace was computed for a thickness h and a distance d of 4km for a dominant period of 15 s. No clear signal from a discontinuity is visible. The different models produce precursors with different amplitudes, the highest amplitude being achieved for a thickness and a distance of half a wavelength, i.e. $\sim$4 km. (b) Sketch of laminated discontinuity model.

thickness of 4 km and a distance between the lamellae of 4 km is able to generate large precursor amplitudes (amplitude ratio $A_{P210P}/A_{PP} \approx 8$ per cent), the large precursor amplitude for the small impedance contrast being the result of constructive interference. The reflectivity results can be used only qualitatively, but they show that models of a laminated reflector exist which are detectable by 1 Hz short-period data, whereas they are transparent for longer periods. The model producing the largest amplitudes has a thickness and a distance of approximately half a wavelength λ ($\lambda \approx 8$ km). As the reflectivity method allows only one-dimensional variations of the seismic parameters, these tests cannot distinguish between a continuous laminated discontinuity and localized embedded bodies.

The fk-analysis does not allow an unambiguous conclusion to be drawn on the velocity contrast across the reflector. To give lower bound estimates on the velocity jump, forward modelling was used. Due to the indirect method of modelling no absolute model of the Lehmann discontinuity can be given. The synthetic modelling gives models where the underside reflections are strong enough to be detected by the sliding-window fk-analysis. The impedance of the Lehmann discontinuity at the reflection points where it is detected is most likely higher or the discontinuity sharper than our modelling indicates. The models are one-dimensional and therefore can not account for the strong topography which is indicated by the strong depth differences of the discontinuity.

For different models synthetic seismograms were computed using the reflectivity method (Müller 1985). Two parameters were varied: (i) the velocity change across the discontinuity and (ii) the thickness of the discontinuity. Most *PP* studies use the $h \approx \lambda/2$ estimate derived for $P'P'$ precursors (Richards 1972) to relate the maximum thickness h of a discontinuity with the wavelength λ used to study the discontinuity. The results of $P'P'$ studies cannot be simply transferred to those of the *PP*-phase due to the different incident angles of the waves at the discontinuity. $P'P'$ has nearly vertical (0°) incidence at the discontinuity, whereas *PP* shows angles of $\sim$40°.

The effect of a gradient zone with changing velocity and density over a depth interval on the underside reflection from the *L* is shown in Fig. 12. The models used for the calculation

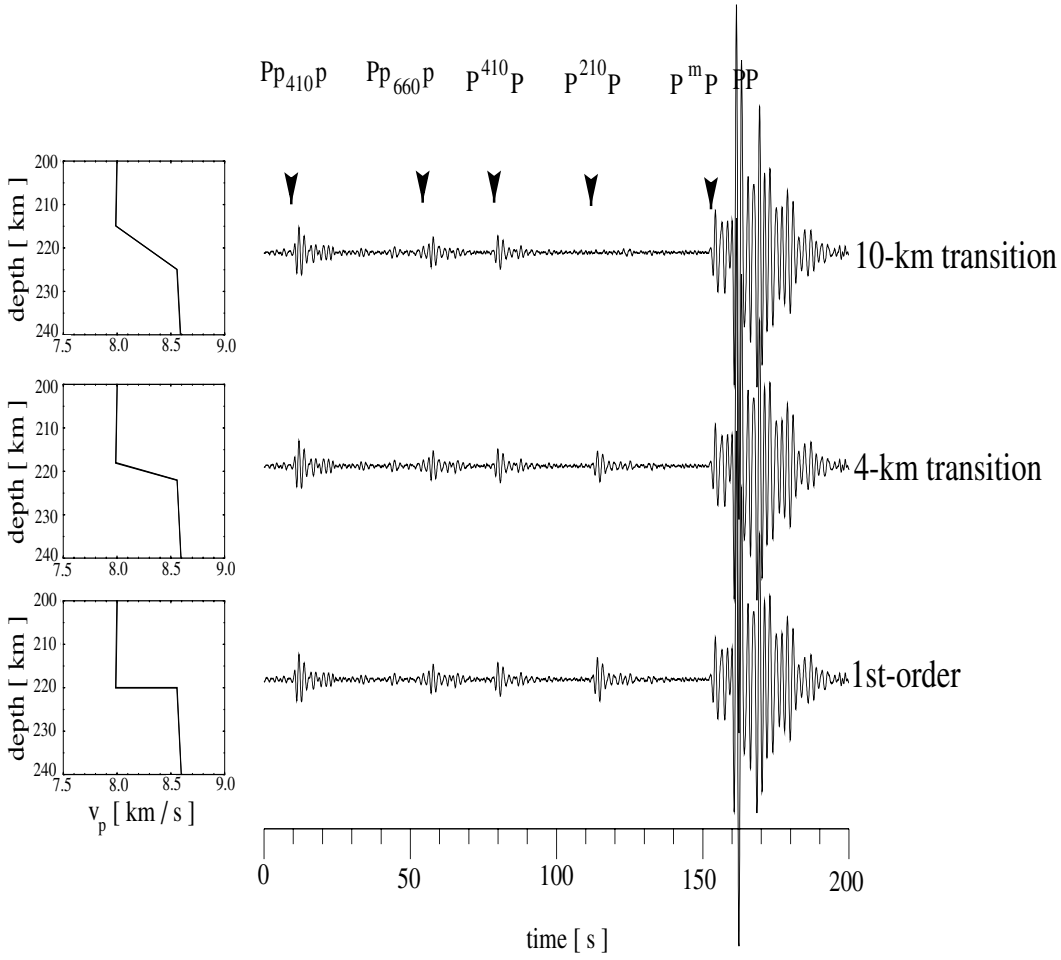

Figure 12. Effect of increasing thickness of a gradient zone of the L on the amplitude of the underside reflection for short-period waves ($T_{\mathrm{dom}} = 1$ s). The right hand side shows three seismogram traces with increasing width from a sharp discontinuity (1st-order) to a 10-km gradient. The corresponding velocity models used to compute the synthetic seismograms are shown on the left hand side. The velocity and density changes of PREM were used. The arrivals of PP, P^mP (Moho reflection), $P^{410}P$, $Pp_{410}p$, $Pp_{660}p$, and $P^{220}P$ are marked atop the traces. The $P^{220}P$ onset is clearly visible for the 1st-order discontinuity, but invisible on the trace for the 10 km gradient.

of the synthetic seismograms (right) are shown on the left. The discontinuity structure is varied from a sharp discontinuity (1st-order discontinuity) to a 10 km wide gradient zone. The v_P and v_S velocity change corresponds to the velocity jump at the 220 km discontinuity in PREM (Dziewonski & Anderson 1981). The seismograms are short-period with a dominant period of 1 s, filtered using a 4th-order band-pass with cut off frequencies of 0.5 Hz and 1.4 Hz, and are normalized to PP. The arrivals of PP and some under- and upperside reflections are marked. The underside reflection from the L is clearly visible in the seismogram trace calculated for a sharp discontinuity. The amplitude in the trace for a 4 km gradient is reduced but still visible. No underside reflection from the L can be detected in the seismogram computed for a 10 km gradient.

A more detailed study of the influence of the thickness and impedance contrast of the L on PP precursors is shown in Figs 13a and b, respectively. The seismograms were processed as described in Fig. 12. The P-wave impedance Z_p ($Z_p = v_p \cdot \rho$) was varied from 0.93 to 9.58 per cent and the gradient thickness was varied from 0 to 20 km.

Fig. 14 shows amplitude ratios of $P^{210}P$ versus PP as a function of gradient thickness (Fig. 14a) and impedance contrast (Fig. 14b) for the synthetic seismograms shown in Fig. 13.

The amplitude ratio was determined using the mean amplitude ratios ($P^{210}P/PP$) of the single traces of 18 stations in YKA configuration for a distance of $\Delta = 100^\circ$. The amplitude ratios are used to estimate the thickness and the impedance contrast of the discontinuity. This is done by comparing the synthetic amplitude ratios with the maximum resolution of the fk-analysis. For the resolution, the amplitude ratios of the precursor and the PP arrival are calculated from real YKA recordings. This amplitude ratio is marked by the dashed line. The resolution tests in Fig. 6 show that the sliding-window fk-analysis is able to resolve a coherent signal with amplitudes of 50–70 per cent compared to the noise in a single trace. These thresholds are marked by the solid horizontal lines. The range of detectable minimum values of impedance change (Fig. 14a) and maximum gradient thickness (Fig. 14b) using the sliding-window fk-analysis are indicated by the vertical dashed lines. For Fig. 14a the impedance contrast was fixed at the PREM value for the L ($\Delta v_p = 7.12$ per cent and $\Delta\rho = 2.2$ per cent) and for Fig. 14b a sharp discontinuity was assumed and the impedance change was varied. This analysis indicates that a discontinuity thinner than ~ 7 km and a minimum P-wave impedance contrast of ~ 5 per cent–6.5 per cent are required to produce reflections detectable by the sliding-window fk-analysis.

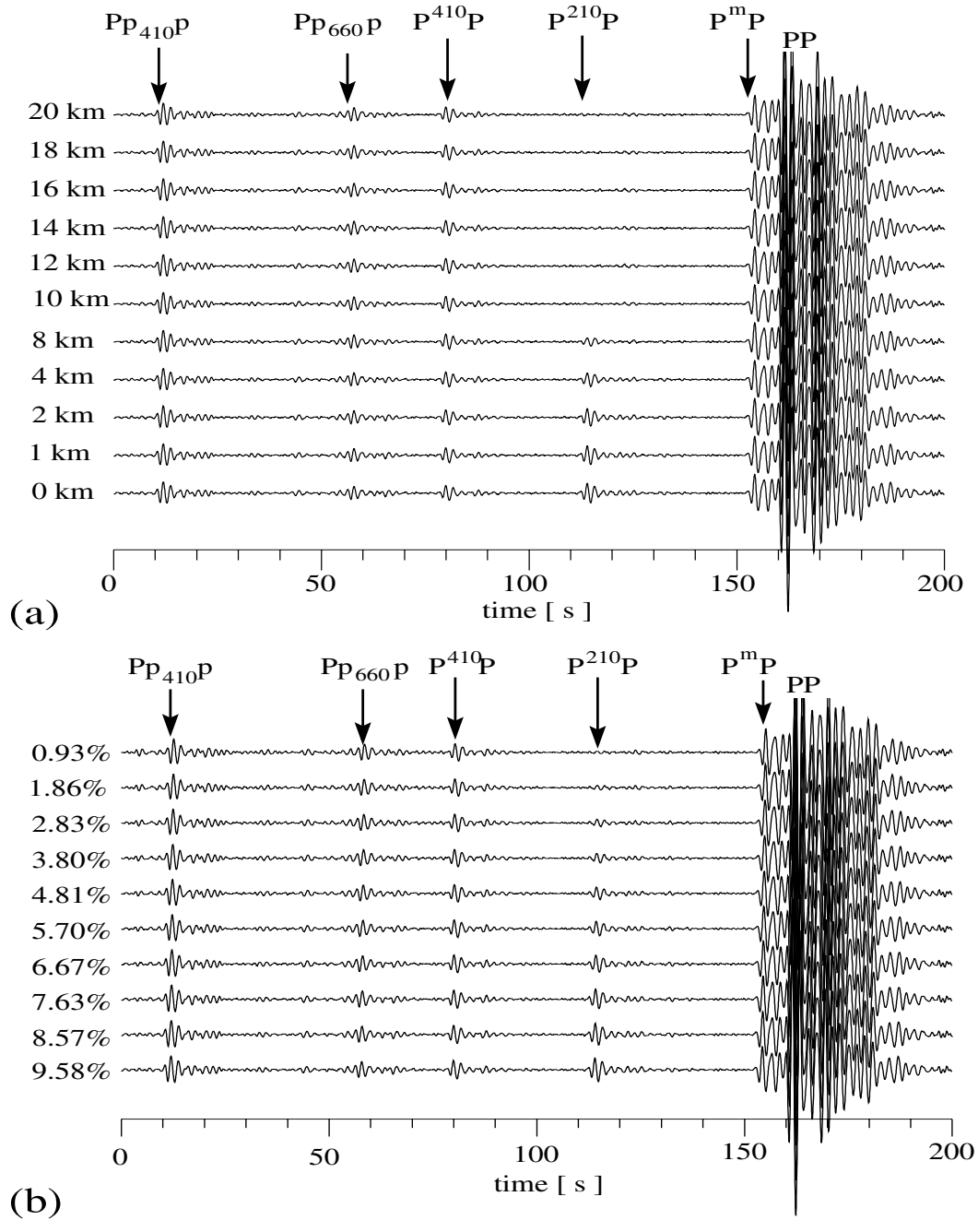

Figure 13. (a) Synthetic seismograms computed to test the influence of the gradient thickness on the precursor's amplitudes. All synthetic seismograms are band-pass filtered using a fourth-order Butterworth bandpass with cut-off frequencies of 0.5 Hz and 1.4 Hz, and the amplitudes are normalized on *PP*. The thickness of the discontinuity is varied between 0 km and 20 km. The visibility of the Lehmann discontinuity underside reflection vanishes between gradient thicknesses of 8 km to 10 km. (b) Synthetics with varying *P*-wave impedance contrast. The impedance contrast is varied from 0.93 per cent to 9.58 per cent.

This is equivalent to a *P*-wave velocity contrast of ~4.3 per cent, assuming the PREM density contrast.

A trade-off exists between the thickness and the *P*-wave velocity change. A 10 km broader gradient zone would result in a ~18 per cent smaller maximum impedance change. For all models presented here, the *S*-velocity at the *L* was changed in the same way as the *P*-velocity, though a variation of this parameter has a minor influence on the amplitudes of the $P^{210}P$ phases. A 5 per cent change of the *S*-velocity produces a 2.6 per cent change of the *PP* reflection coefficient.

The minimum *P*-velocity change of ~4.3 per cent found in this study is in good agreement with velocity changes of 3.5–4.5 per cent across the *L* found by studying direct *P*-waves (Anderson 1979). The value for the *L* given by PREM (~7.1 per cent) (Dziewonski & Anderson 1981) is slightly larger.

The mineralogical model of the *L* with a change from anisotropic to isotropic material as source of the discontinuity predicts a thickness of ~20 km due to the change of the creep mechanism from dislocation to diffusion creep (Karato 1992). This thickness is based on mineralogical observations only and

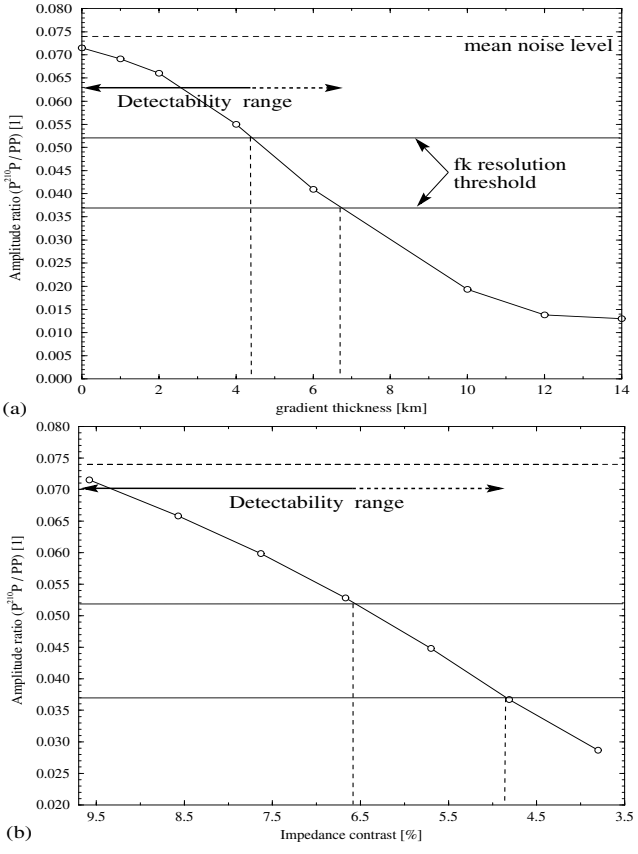

Figure 14. Amplitude ratios of the synthetic seismograms computed with the reflectivity method. For the computation a combined model of PREM (Dziewonski & Anderson 1981) and ek1 (Estabrook & Kind 1996) was used. The PREM model was used above 271 km depth, while ek1 was used below. To estimate the thickness of the discontinuity and the *P*-wave velocity jump across the discontinuity, these parameters were varied. The amplitude ratio of $P^{210}P$ relative to *PP* in single traces versus the variable parameter is displayed. The mean amplitude ratio of *PP* relative to the noise amplitude of the data set is marked by the horizontal dashed line. (a) Variation of gradient thickness of the L. The horizontal solid lines mark the 50–70 per cent resolution level of the data noise level. This resolution level below the noise level was found by the synthetic resolution tests shown in Fig. 6. This synthetic test indicates that L with a thickness of less than about 7 km can be detected. (b) Variation of the impedance change across the L. The impedance change is given in per cent. This test indicates that a *P*-wave impedance contrast of larger than 5 per cent can be detected.

contains a large error as a result of the uncertainty of the activation volume of the two deformation processes and might also be temperature dependent (Karato & Wu 1993). Additionally, the unknown grain size of deformed rocks influences the transition width (Karato 1992). Nevertheless, it is uncertain whether a sharp discontinuity can be explained by the change of creep mechanism or by the onset of partial melt.

The region studied has very little variation in lithospheric age (100 ± 5 Myr) and the reflection points mostly sample old oceanic lithosphere. Therefore, a dependency of the discontinuity depth or discontinuity structure from lithospheric age cannot be studied. The results shown in Fig. 10 indicate no strong influence of the cold, fast subducting Kuril slab on the discontinuity depth, excluding a temperature controlled mechanism for the L.

5 CONCLUSIONS

As shown in Figs 5, 6 and 7, the detection of P^dP with short-period arrays is possible. The results presented here focus on a reflector at a depth of $\sim$200 km, which may be the Lehmann discontinuity beneath oceanic regions. The changes in reflection depth could either be due to strong topography, in contradiction to previous studies, or due to localized inhomogeneities in this depth interval. The *PP* reflection points sample the upper mantle beneath old oceanic lithosphere with little age variation; therefore, the influence of the cooling lithosphere on the reflector cannot be studied. On the other hand, the Kuril subduction zone does not influence the depth of the *L* noticeably. A temperature controlled mechanism for the *L* can therefore most likely be ruled out.

Using synthetic seismograms, it is possible to study different models of the reflector in one dimension and to give upper limits of the impedance change across the discontinuity and of the sharpness of the discontinuity. A lamination of the reflector could explain the detection in the short-period studies and the lack of $P^{210}P$ phases in the stack of long-period data. The reflector must be sharper than $\sim$7 km and show a minimum impedance contrast of $\sim$5–6.5 per cent, assuming a sharp discontinuity, to be in agreement with our data. This impedance contrast is equivalent to a *P*-wave velocity change of 4.3 per cent assuming the PREM density change.

No detailed answer on the nature of the discontinuity can be given by this study, but some hints can be given by the analysis of short-period data. Models including a LVZ with partial melt at the bottom or the boundary between two regions with different anisotropy structure are discussed. Calculations of *PP* reflection coefficients for isotropic/isotropic and isotropic/anisotropic discontinuities at 220 km (using PREM parameters) yield similar results for incident angles of about 50° (Rümpker, personal communication 2000). This indicates that the *PP* reflections are insensitive to variations in anisotropy across the discontinuity (which might result from changes in plate motion) and that we cannot discriminate between the two types of boundaries from our observations. This result would corroborate the interpretation of the *L* as the lower boundary of the LVZ.

The use of short-period array data and the application of array methods allow a much better resolution of the structure and the depth of the different discontinuities than previously obtained from long-period seismograms. In addition, the use of *PP* underside reflections enables the study of regions where no sources or receivers are located using some of the short-period arrays installed globally.

ACKNOWLEDGMENTS

We thank the staff, especially Bill Shannon, of the Data Centre of the Geological Survey of Canada (GSC) in Ottawa for the help in retrieving the data, the GSC for the opportunity to use the YKA Dataset and the German Academic Exchange Service (DAAD) for a travel grant to collect the data. The maps are produced using GMT software by Wessel and Smith. We thank Klaus Stammler for his Seismic Handler software. Georg Rümpker was very helpful with his calculations of reflection coefficients for different anisotropic models. Comments by Jim Gaherty and discussions with Andrew Fredericksen, Justin Revenaugh and Joachim Ritter helped to improve the manuscript. We thank two anonymous reviewers for their comments.

REFERENCES

Aki, K. & Richards, P.G., 1980. *Quantitative seismology theory and methods,* Vol. II, Freeman and Company, San Francisco.

Anderson, D.L., 1979. The deep structure of continents, *J. geophys. Res.,* **84,** 7555–7560.

Berkhout, A.J., 1984. *Seismic resolution: resolving power of acoustical echo techniques,* Geophysical Press, London.

Bina, C.R., 1991. Mantle discontinuities, *Rev. Geophys. Suppl.,* **10,** 783–793.

Bina, C.R. & Wood, B.I., 1984. The eclogite to garnet transition—experimental and thermodynamical constraints, *Geophys. Res. Lett.,* **11,** 955–958.

Birch, F., 1952. Elasticity and constitution of the Earth's interior, *J. geophys. Res.,* **57,** 227–286.

Bolt, B.A., O'Neill, M. & Qamar, A., 1968. Seismic waves near 100°: Is structure in core or upper mantle responsible?, *Geophys. J. R. astr. Soc.,* **16,** 475–487.

Capon, J., 1973. Signal processing and frequency-wavenumber spectrum analysis for a large aperture seismic array, *Methods in Computational Physics,* Vol. 13, pp. 2–59 Academic Press, New York.

Chaljub, E. & Tarantola, A., 1997. Sensitivity of *SS* precursors to topography on the upper-mantle 660-km discontinuity, *Geophys. Res. Lett.,* **24,** 2613–2616.

Chevrot, S., Vinnik, L. & Montagner, J.-P., 1999. Global-scale analysis of the mantle Pds phases, *J. geophys. Res.,* **104,** 20 203–20 219.

Cleary, J.R., King, D.W. & Haddon, R.A.W., 1975. P-wave scattering in the Earth's crust and upper mantle, *Geophys. J. R. astr. Soc.,* **43,** 861–872.

Davis, J.P., Kind, R. & Sacks, I.S., 1989. Precursors to *P′P′* re-examined using broad-band data, *Geophys. J. Int.,* **99,** 595–604.

Dziewonski, A.M. & Anderson, D.L., 1981. Preliminary reference Earth model, *Phys. Earth planet. Inter.,* **25,** 297–356.

Engdahl, E.R., Hilst, R.v.d. & Buland, R.P., 1998. Global teleseismic earthquake relocation with improved travel times and procedures for depth determination, *Bull. seism. Soc. Am.,* **88,** 772–743.

Estabrook, C.H. & Kind, R., 1996. The nature of the 660-km upper mantle seismic discontinuity from precursors to the *PP* phase, *Science,* **274,** 1179–1182.

Flanagan, M.P. & Shearer, P.M., 1998. Global mapping of topography on transition zone velocity discontinuities by stacking *SS* precursors, *J. geophys. Res.,* **103,** 2673–2692.

Flanagan, M.P. & Shearer, P.M., 1999. A map of topography of the 410-km discontinuity from *PP* precursors, *Geophys. Res. Lett.,* **26,** 549–552.

Gaherty, J.B. & Jordan, T.H., 1995. Lehmann discontinuity as the base of an anisotropic layer beneath continents, *Science,* **268,** 1468–1471.

Gaherty, J.B., Kato, M. & Jordan, T.H., 1999. Seismological structure of the upper mantle: a regional comparison of seismic layering, *Phys. Earth planet. Int.,* **110,** 21–41.

Goncz, J.H. & Cleary, J.R., 1976. Variations in the structure of the upper mantle beneath Australia from Rayleigh wave observations, *Geophys. J. R. astr. Soc.,* **44,** 507–516.

Gudmundsson, O. & Sambridge, M., 1998. A regionalised upper mantle (RUM) seismic model, *J. geophys. Res,* **103,** 7121–7136.

Hales, A.L., Muirhead, K.J. & Rynn, J.M., 1980. A compressional velocity distribution for the upper mantle, *Tectonophysics,* **63,** 309–348.

Harjes, H.-P. & Henger, M. 1973. Array Seismologie, *Zeitschr. f. Geophysik,* **21,** 865–905.

Karato, S.-I., 1992. On the Lehmann discontinuity, *Geophys. Res. Lett.,* **19,** 2255–2258.

Karato, S.-I. & Wu, P. 1993. Rheology of the upper mantle: A synthesis, *Science,* **260,** 771–778.

Kennett, B.L.N. & Engdahl, E.R., 1991. Traveltimes for global earthquake location and phase identification, *Geophys. J. Int.,* **105,** 429–465.

Kind, R. & Vinnik, L.P., 1988. The upper mantle discontinuities underneath the GRF array from *P*-to-*S* converted phases, *J. Geophys.,* **62,** 138–147.

Lehmann, I., 1959. Velocities of longitudinal waves in the upper part of the Earth's mantle, *Ann. Geophys.,* **15,** 93–118.

Lehmann, I., 1961. S and the structure of the upper mantle, *Geophys. J. R. Astron. Soc.,* **4,** 124–138.

McFadden, P.L., Drummond, B.J. & Kravis, S., 1986. The Nth-root stack: Theory, applications, and examples, *Geophysics,* **51,** 1879–1892.

Müller, G., 1985. The reflectivity method: a tutorial, *J. Geophys.,* **58,** 153–174.

Müller, D., Roest, W.R., Royer, J.-Y., Gabagan, L.M. & Sclater, J.-G., 1997. Digital isochrons of the world's ocean floor, *J. geophys. Res.,* **102,** 3211–3214.

Muirhead, K.J. & Datt, T., 1976. The n-th root process applied to seismic data, *Geophys. J. R. astr. Soc.,* **47,** 197–210.

Neele, F. & deRegt, H., 1999. Imaging upper-mantle discontinuity topography using underside-reflection data, *Geophys. J. Int.,* **137,** 91–106.

Neele, F., deRegt, H. & VanDecar, J., 1997. Gross errors in upper-mantle discontinuity topography from underside reflection data, *Geophys. J. Int.,* **129,** 194–204.

Revenaugh, J.S. & Jordan, T.H., 1991a. Mantle layering from ScS reverberations, 1. Waveform inversion of zeroth-order reverberations, *J. geophys. Res.,* **96,** 19 749–19 762.

Revenaugh, J.S. & Jordan, T.H., 1991b. Mantle layering from ScS reverberations, 2. The transition zone, *J. geophys. Res.,* **96,** 19 763–19 780.

Revenaugh, J.S. & Jordan, T.H., 1991c. Mantle layering from ScS reverberations, 3. The upper mantle, *J. geophys. Res.,* **96,** 19 781–19 810.

Richards, P.G., 1972. Seismic waves reflected from velocity gradient anomalies within the Earth's upper mantle, *Zeitschr. f. Geophys.,* **38,** 517–527.

Ringwood, A.E., 1975. *Composition and Petrology of the Earth's mantle,* McGraw Hill, New York.

Ringwood, A.E., 1991. Phase transformations and their bearings on the constitution and dynamics of the mantle, *Geochim. Cosmochim. Acta,* **55,** 2083–2110.

Rost, S., 2000. A study of the Earth's upper mantle discontinuities in the Pacific using a short-period array, *Göttinger Beiträge zur Physik,* **Bd. 7,** Duehrkohp und Radicke, Göttingen.

Rost, S. & Thomas, C., 2001. Array seismology: Methods and Applications, *Rev. Geophys.,* in review.

Rost, S. & Weber, M., 2001. The upper mantle transition zone in the Pacific as determined by short-period array data, submitted to *J. geophys. Res.,* in review.

Sacks, I.S., Snoke, J.A. & Husebye, E.S., 1979. Lithosphere thickness beneath the Baltic shield, *Tectonophysics,* **56,** 101–110.

Shearer, P.M., 1991. Constraints on upper mantle discontinuities from observations of long-period reflected and converted phases, *J. geophys. Res.,* **96,** 14 147–18 182.

Vidale, J.E. & Benz, H.M., 1992. Upper-mantle seismic discontinuities and the thermal structure of subduction zones, *Nature,* **356,** 678–683.

Vinnik, L.P., 1977. Detection of waves converted from *P* to SV in the mantle, *Phys. Earth planet. Inter.,* **15,** 39–45.

Weber, M., 1990. Subduction zone, their influence on travel times and amplitudes of *P*-waves, *Geophys. J. Int.,* **101,** 529–544.

Weber, M. & Wicks, C.W., 1996. Reflections from a distant subduction zone, *Geophys. Res. Lett.,* **23,** 1453–1456.

Woodward, R. L. & Masters, G. 1991. Global upper mantle structure from long-period differential travel times, *J. geophys. Res.,* **96,** 6351–6377.

Wright, C. & Muirhead, K.J., 1969. Longitudinal waves from the Novaya Zemlya nuclear explosion of October 27, 1966, recorded at the Warramunga seismic array, *J. geophys. Res.,* **74,** 2034–2048.